

JGR Solid Earth

RESEARCH ARTICLE

10.1029/2022JB025635

Key Points:

- Various flow processes within karst aquifers generate seismic signals that can be recorded with surface monitoring stations
- Largest signals during injection experiments arise from water impact on surface spring opening and with subsurface water-filled passage
- Natural recharge event produced largest seismic signals from two regions, including the area of the subsurface sump

Supporting Information:

Supporting Information may be found in the online version of this article.

Correspondence to:

S. L. Bilek,
susan.bilek@nmt.edu

Citation:

Bilek, S. L., Luhmann, A. J., Grapenthin, R., Woo, H. B., & Gochenour, J. A. (2023). Capturing seismic signals from karst aquifer injection experiments and a natural recharge event. *Journal of Geophysical Research: Solid Earth*, 128, e2022JB025635. <https://doi.org/10.1029/2022JB025635>

Received 15 SEP 2022
Accepted 28 MAR 2023

Author Contributions:

Conceptualization: S. L. Bilek
Data curation: S. L. Bilek
Formal analysis: S. L. Bilek, A. J. Luhmann, Han Byul Woo, J. A. Gochenour
Funding acquisition: S. L. Bilek, A. J. Luhmann, R. Grapenthin
Methodology: S. L. Bilek
Project Administration: S. L. Bilek, A. J. Luhmann
Resources: A. J. Luhmann
Supervision: S. L. Bilek, A. J. Luhmann
Writing – original draft: S. L. Bilek, A. J. Luhmann, R. Grapenthin

© 2023. American Geophysical Union.
All Rights Reserved.

Capturing Seismic Signals From Karst Aquifer Injection Experiments and a Natural Recharge Event

S. L. Bilek¹ , A. J. Luhmann² , R. Grapenthin³ , Han Byul Woo¹, and J. A. Gochenour¹ 

¹Earth and Environmental Science Department, New Mexico Institute of Mining and Technology, Socorro, NM, USA, ²Department of Earth and Environmental Science, Wheaton College, Wheaton, IL, USA, ³Department of Geosciences, Geophysical Institute, University of Alaska Fairbanks, Fairbanks, AK, USA

Abstract Variations in subsurface flow processes through a karst aquifer that feeds Bear Spring in southeastern Minnesota were captured on a temporary seismic network during injection experiments and a natural recharge event. Each experiment involved injecting ~13,000 L of water into an overflow spring, and the natural event was triggered by a large rainstorm of ~70 min in duration. During the injection experiments, the largest amplitude signals in the ground velocity seismograms occurred as the water first fell onto the rock at the overflow spring and as the large slug of water reached a sump or water-filled passage. During the natural rainstorm event, the overflow spring began flowing and total spring discharge (perennial emanation points and the overflow spring) increased from ~100 to 300 L/s. Seismic signals during and following the rain event include broadband noise from raindrops impacting the ground, as well as large amplitude signals while water levels rose; the latter occurred over a 5-s period, producing multiple pulses of ground motion up to ~0.5 mm/s. Based on seismic array analysis, high frequency signals during the natural recharge event and one of the injection experiments are largely sourced from south of the array, where a sump exists and the conduit orientation changes, but additional modeling is required to further understand which of a set of possible mechanisms is mostly likely the cause of these seismic signals.

Plain Language Summary Karst aquifers provide important subsurface water storage and are dynamic hydrologic systems that can respond quickly to heavy rainfall, yet understanding their subsurface architecture and how it impacts flow can be difficult. We conducted a joint hydrologic and geophysics study above a mapped karst aquifer to investigate possible geophysical signals associated with changes in water levels and flow within the aquifer. Here, we present new observations of seismic signals generated within a karst aquifer during both human-generated injection experiments as well resulting from a large natural rain event. We find large amplitude seismic signals associated with water hitting the base of the spring and impacting a subsurface fluid-filled passage. These seismic observations can form the basis of future studies on how these signals may be generated within the karst system.

1. Introduction

The expanding field of environmental seismology has provided novel opportunities to study a variety of Earth surface processes that are complementary to traditional monitoring methods while enabling entirely new observations that were not previously possible (e.g., Burtin et al., 2016; Cook & Dietz, 2022 for reviews). There are a wide range of environmental use cases, but we focus here on those applied to aquifer properties and water flow. Recent seismic data analysis has been used to detect changes in water table, groundwater storage (e.g., Almagro Vidal et al., 2021; Clements & Denolle, 2018; Garambois et al., 2019; Kim & Lekic, 2019) and water saturation in karst systems (Fores et al., 2018) using temporal changes in seismic velocity. Other studies demonstrate that seismic monitoring of surface rivers and streams enables characterization of bedload transport, turbulence, and other flow processes (e.g., Anthony et al., 2018; Barrière et al., 2015; Burtin et al., 2008, 2010, 2011; Ronan et al., 2017; Schmandt et al., 2013; Smith & Tape, 2019). In addition, environmental seismology has been used to identify many glacial processes including subglacial drainage activity (e.g., Aso et al., 2017; Aster & Winberry, 2017; Bartholomäus et al., 2015; Lindner et al., 2020; Nanni et al., 2020), as well as air dynamics (Podolskiy, 2020), fracturing (Podolskiy et al., 2018), subglacial flow structure and size (Gimbert et al., 2016; Vore et al., 2019; Zhan, 2019), and tracking of subglacial flood fronts (Eibl et al., 2020).

Other possible targets for seismic analysis of flow are karst landscapes, which form when soluble rocks such as carbonates react with CO_2 /acid to dissolve (e.g., Ford & Williams, 2007; Hartmann et al., 2014; White, 2002). This produces features at the surface such as sinking streams, sinkholes, and springs, but the dissolution below the surface enlarges fractures and bedding planes to produce conduits and caves. Some water may slowly flow through the soil and rock matrix, but the conduits make karst aquifers dynamic hydrologic systems where water levels may quickly rise and fall in response to precipitation and snowmelt events. This causes significant variability in flow and transport (e.g., Ford & Williams, 2007; Herman et al., 2008; Ravbar, 2013; Vesper & White, 2003), including the activation of additional flow paths (Birk et al., 2014; Mayaud et al., 2014). Karst conduits enable fast flow, such that maximum velocities on the order of km/day have been reported (e.g., Worthington & Ford, 2009). Such conduit flow will have similarities to flow in surface streams (velocities, turbulence, open channel flow) and subglacial systems (full pipe flow, transitions between open channel and full pipe flow, water interacting with rough conduit walls instead of the streambed). Based on the success of seismic studies to characterize flow in both streams and glacial systems, studies of flow in karst may also benefit from seismic data collection and analysis.

When placing all aquifers on a spectrum with respect to water level changes and maximum velocities, karst aquifers are an extreme endmember because of the conduits (e.g., Ford & Williams, 2007). Flow processes in the conduits will likely generate a variety of seismic signals, such as seismic pulses or tremor energy associated with water pressure waves impacting channel walls (e.g., Roeoesli et al., 2016) and tremor signals associated with changes in discharge (e.g., Bartholomaeus et al., 2015; Eibl et al., 2020).

More traditional uses of seismology have focused on characterization of the architecture of a karst system, including the thicknesses of soil and regolith as well as the distribution of the conduit network (and other preferential flow paths), which is typically poorly known. Although conduits are of utmost importance in controlling flow through the system (e.g., Budd & Vacher, 2004; Worthington, 1999; Worthington et al., 2000), many are impossible to enter and are incredibly difficult to locate or characterize using other means. Thus, noninvasive seismic methods have previously been employed to remotely map the location of karst aquifers (e.g., Hiltunen & Cramer, 2008; James et al., 2017; Sumanovac & Weisser, 2001). However, fewer studies have used seismic methods to investigate subsurface karst aquifer flow processes.

We conducted a field study to test whether changes in ground water flow in karst conduits would generate distinct seismic signals recorded on surface seismograph systems. The experiment included controlled water injections that were conducted by pouring water into a dry overflow spring that is directly connected to a mapped subsurface conduit. Additionally, during the experiments, a ~ 5 -cm rainfall event generated large amplitude seismic (~ 1 - μm ground displacement) and hydrologic (200 L/s increase, or a tripling in discharge) signals. Here, we document responses to both the injection experiments and the rainstorm event, which provides additional applications for environmental seismology as an innovative means for noninvasive monitoring of groundwater flow and other processes in karst aquifers.

2. Study Area

We conducted artificial recharge experiments near Bear Spring, which emanates from the Ordovician Prosser Limestone of the Galena Group (Mossler, 2008) and is located west of Eyota, Minnesota, USA (4,869,610N, 557,713E, UTM Zone 15; Figure 1). The current estimated springshed size of Bear Spring is 4.4 km² based on hydrograph analysis (Barry et al., 2020) and ongoing dye tracing work is further refining the springshed extent. Baseflow discharge is generally 0.017–0.034 m³/s, although high flow events may approach ~ 1 m³/s (Barry et al., 2020). The average annual precipitation (1991–2020) for the area of 89 cm (Minnesota Department of Natural Resources, 2021). Bear Perennial Spring (ID 55A0000406 in the Minnesota Karst Features Database (Minnesota Department of Natural Resources, 2022)) is a complex spring system. During our short monitoring period, groundwater discharge occurred from several perennial points, including south of the spring house and from several boils within the spring house. In addition, there was an initially dry overflow spring ~ 60 m south-southwest of Bear Perennial Spring (Bear Overflow Spring (ID 55A0000572 in the Minnesota Karst Features Database (Minnesota Department of Natural Resources, 2022)) 4,869,551N, 557,689E, UTM Zone 15) that began flowing after a large rain event that occurred near the end of the seismic deployment. With a compass and tape survey, we mapped the ~ 1 m diameter cave passage connected to the dry overflow spring a few days before the injection experiments, and the passage generally trends southeast for ~ 20 m until it becomes a sump,

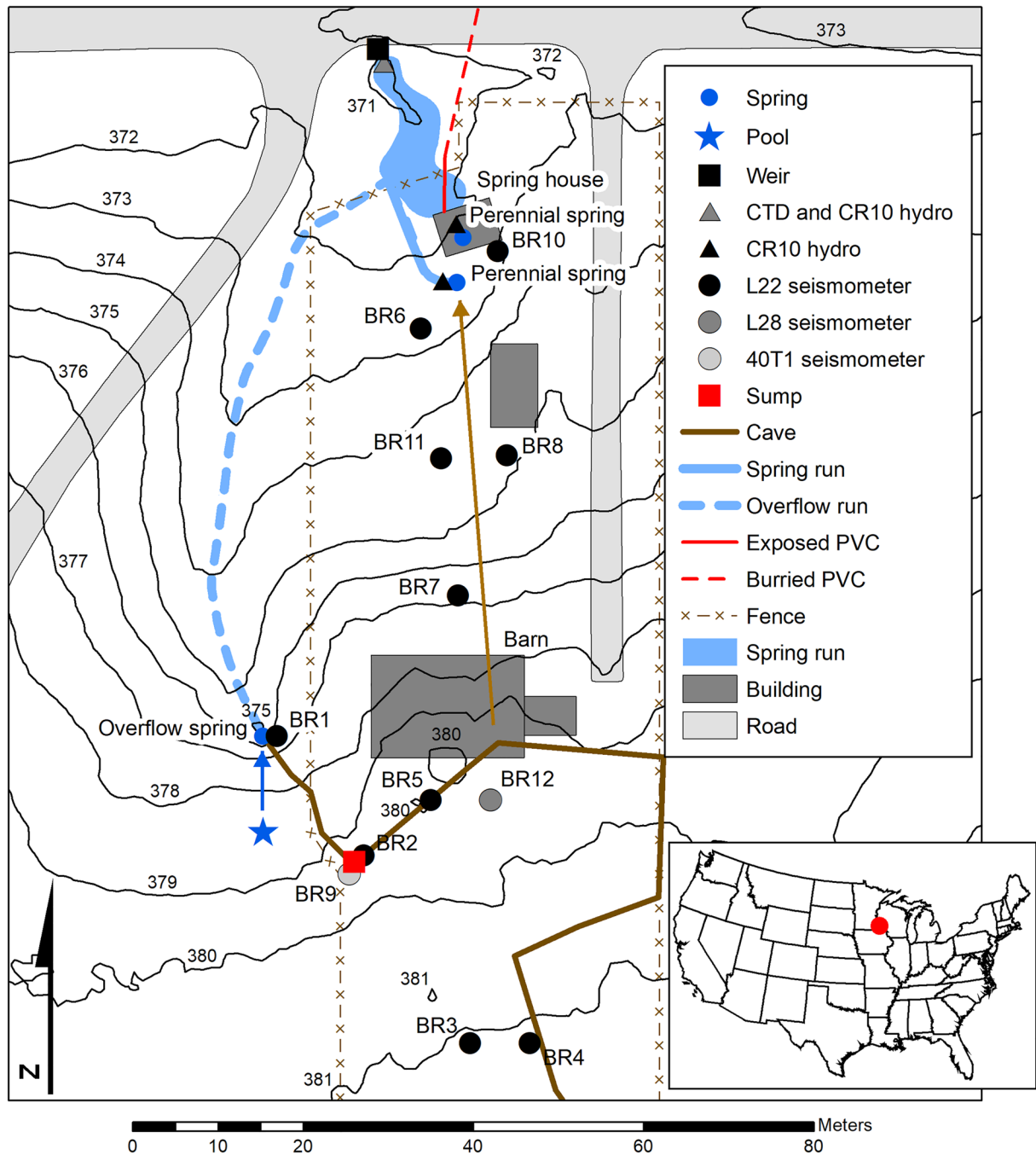


Figure 1. Instrument network layout near Bear Spring, MN, to observe karst aquifer recharge signals. All of the perennial springs and the overflow spring are collectively known as Bear Spring. Sensors include 12 seismometers and hydrologic sensors to capture discharge, electrical conductivity, and temperature changes. The blue arrow indicates the surface flow path from the pool to the overflow spring where water entered a conduit during the first two injection experiments, and the light brown arrow indicates the estimated cave passage to the north. Inset map shows field location in southeastern Minnesota, USA.

where the cave is full of water. During a subsequent visit in the passage under lower flow conditions, the cave map was extended until another sump was encountered. The first two injection experiments caused minimal to little change in the ~ 100 L/s background discharge, but heat, salt, and fluorescent dye served as tracers during the experiments which indicated a direct connection between the injection point at the dry overflow spring and the perennial discharge points of Bear Spring.

Table 1
Pool and Flow Characteristics for Each Injection Experiment

Injection experiment	Start of injection (UTC)	Release time (s)	Salt in pool (kg)	Pool water temperature (°C)	Pool water electrical conductivity (mS/cm)	Flow characteristics
#1	11 June 2016 18:03:50	538	68.82	19.7	14.73	Injection into conduit at the overflow spring; immediately drained into the conduit upon reaching the overflow spring
#2	11 June 2016 22:49:24	96	Residual from previous experiment	11.6	0.893	Injection into conduit at the overflow spring; some ponding occurred
#3	12 June 2016 19:06:20	179	272			Surficial flow along the overflow run

3. Methods

3.1. Experimental Design

An inflatable pool of water (~13,000 L) was emptied twice (injection experiments) into the dry overflow spring to simulate recharge events at two different injection rates on 11 June 2016 (see pool and flow characteristics in Table 1). For each injection experiment, the pool was placed uphill of the dry overflow spring and filled with water pumped from the perennial springs (Figures 1 and S1 in Supporting Information S1). Before the first injection, water was added to the pool during the previous day (10 June), which allowed the water to warm above background spring water temperatures. Salt was also added to increase the electrical conductivity of the water. The first injection experiment started at 18:03:50 UTC on 11 June, where water was slowly released by holding down the northern third of the pool over a duration of 8 min and 58 s. With the relatively slow release, the water immediately drained upon reaching the dry overflow spring. In addition, fluorescent dye solution was poured into the injection stream of water as it entered the overflow spring at 18:04:11 UTC, and it first appeared at the perennial spring at 18:19:44 UTC, confirming the direct connection between the two features.

To maximize the ability to see seismic signals from flow associated with the pool water injection, all field activity stopped for ~20 min. Following this stoppage of activity, the pool was filled again with little time for the water temperature to rise significantly above background spring water temperature before the second injection experiment. No salt was added to the second pool of water. The second injection experiment started at 22:49:24 UTC, and water was released rapidly for 1 min and 36 s. The rapid release resulted in initial ponding at the dry overflow spring that quickly drained when the injection period ended.

Field activity was again stopped following the second injection experiment to reduce human-induced seismic signals, and then the pool was filled with water and salt for a third and final injection experiment that was planned for the following day. However, rain delayed the final experiment, and the dry overflow spring started flowing sometime between 13:13 and 13:40 UTC on 12 June because of the rain runoff. This natural precipitation event significantly increased discharge of the entire spring system (i.e., perennial springs and the previously dry overflow spring). We did not monitor for precipitation at the field site, but the Rochester International Airport, ~19 km to the southwest, recorded 0.05 in (0.13 cm) of rain the morning of 12 June 2016, while the Winona Municipal Airport, ~48 km to the east, recorded 1.61 in (4.09 cm; Midwestern Regional Climate Center, 2021). In addition, a weather station on Weather Underground (KMNPLAIN3, <https://www.wunderground.com/dashboard/pws/KMNPLAIN3/graph/2016-06-12/2016-06-12/daily>, last accessed 7 June 2022, in Plainview, MN ~23 km north of our site) recorded 1.98 inches (5.0 cm) of rain that morning. When it became apparent that spring discharge would not recede quickly, the final pool was emptied and released in 2 min and 59 s, beginning at 19:06:20 UTC on 12 June. Because the overflow spring was still flowing, water from the pool mixed with water discharging from the overflow spring and flowed along the overflow run rather than underground.

3.2. Instrumentation Network

We deployed sensors to capture both seismic and hydrologic responses from our injection experiments. We installed 12 seismometers (one Guralp CMG-40T1, flat velocity response between 1 and 100 Hz, 10 Sercel L22 with flat velocity response above 2 Hz and one Sercel L28 with flat velocity response above 4.5 Hz) with RT-130 digitizers, all loaned from the IRIS-PASSCAL Instrument Center. Seismic data were recorded at 500 Hz. These instruments were located above both mapped and assumed conduit locations, with two seismometers above the mapped sump. Seismic sensors were buried in shallow (<0.5 m) holes within soil overlying the Prosser Limestone. All seismic data are archived with the IRIS Data Management Center under network code XK (Bilek, 2016).

One Van Essen CTD-Diver measured water level (after compensation for atmospheric pressure using a barometric pressure sensor deployed on-site), temperature, and electrical conductivity and was attached to a fencepost driven into the spring run just upstream of the weir (Figure 1). One Campbell Scientific CR10 data logger measuring the same parameters with a Campbell Scientific 247-L conductivity/temperature probe and a vented Druck PDCR 830 pressure transducer was installed right next to the CTD-Diver, and two other Campbell CR10 loggers were installed in the spring house and at the far upstream perennial spring emanation (both measuring electrical conductivity and temperature with a Campbell Scientific 247-L conductivity/temperature probe). To convert water level to discharge, a 120° v-notch weir was installed downstream of all data loggers and at the upstream end of the culvert (Figure 1). Additionally, a salt trace discharge measurement was conducted at ~16:05 UTC on June 12 and used to calibrate water levels with respect to the weir.

3.3. Seismic Data Analysis

The primary goal of the project was to record seismic signals associated with changes in water flow within the karst conduit system. The seismic data provide a time series of ground motion, and we describe here when large amplitude ground motions, relative to background levels, occurred during the experiment. We can extract additional information from the seismic data related to power contained in different frequencies of ground motion. These spectral characteristics of the data can help with interpretation of the signals as observed in other environmental seismology studies. Additionally, we can use standard array processing techniques such as frequency-wavenumber (F-K) analysis to estimate the source locations of different seismic signals (e.g., Rost & Thomas, 2002).

As a first step in the processing, we used standard instrument corrections to convert the raw seismic time series (units of counts) into ground velocity (units of m/s) by removing the defined instrument response, data mean and linear trend using tools and workflows in the ObsPy computation package (Beyreuther et al., 2010; Megies et al., 2011). Converting the ground velocity time series into the frequency domain using Fourier transforms allows us to represent the data in spectrograms, showing the seismic power at each frequency over time. These spectrograms were computed for the full experiment time period using the ObsPy spectrogram commands with defined 5-s windows and 10% window overlaps (Figures 2 and S2–S13 in Supporting Information S1). For the time windows around the injection experiments and key portions of the rainstorm, the time resolution of the Fourier transform-based spectrograms is too limited, so in those cases we used a continuous wavelet transform to improve the time resolution of our spectral analysis (e.g., Lapins et al., 2020; Sinha et al., 2005). For these injection experiment and rain event-specific windows, we implemented the PyCWT Python module (version 0.2.0a22, Krieger et al., 2022) for continuous wavelet spectral analysis, using a Morlet mother wavelet. Parameterization of the Morlet wavelet is often described in terms of scales (e.g., Torrence & Compo, 1998), and here we use a starting scale of 0.004 s (smallest scale), spacing between the scales of 12 (12 suboctaves per octave), and seven powers of two to reflect the largest scale. These defined scales are generally related to frequency in Fourier analysis, with generally smaller scales defining a more compressed wavelet useful to characterize higher frequency signals.

Power spectral density (PSD) describes the seismic power within a defined frequency range and time period, allowing for comparison of power between various time periods. We calculated the PSD for defined windows of hydrologic interest using Welch's method (Welch, 1967) with 95% window overlap and number of points in powers of two appropriate for the window length, 2^{12} points (or 8.192 s) for each time window length in applications with the total time >30 s and 2^7 points (0.256 s) for the focused windows (2.5 s total time) around the natural event large peaks.

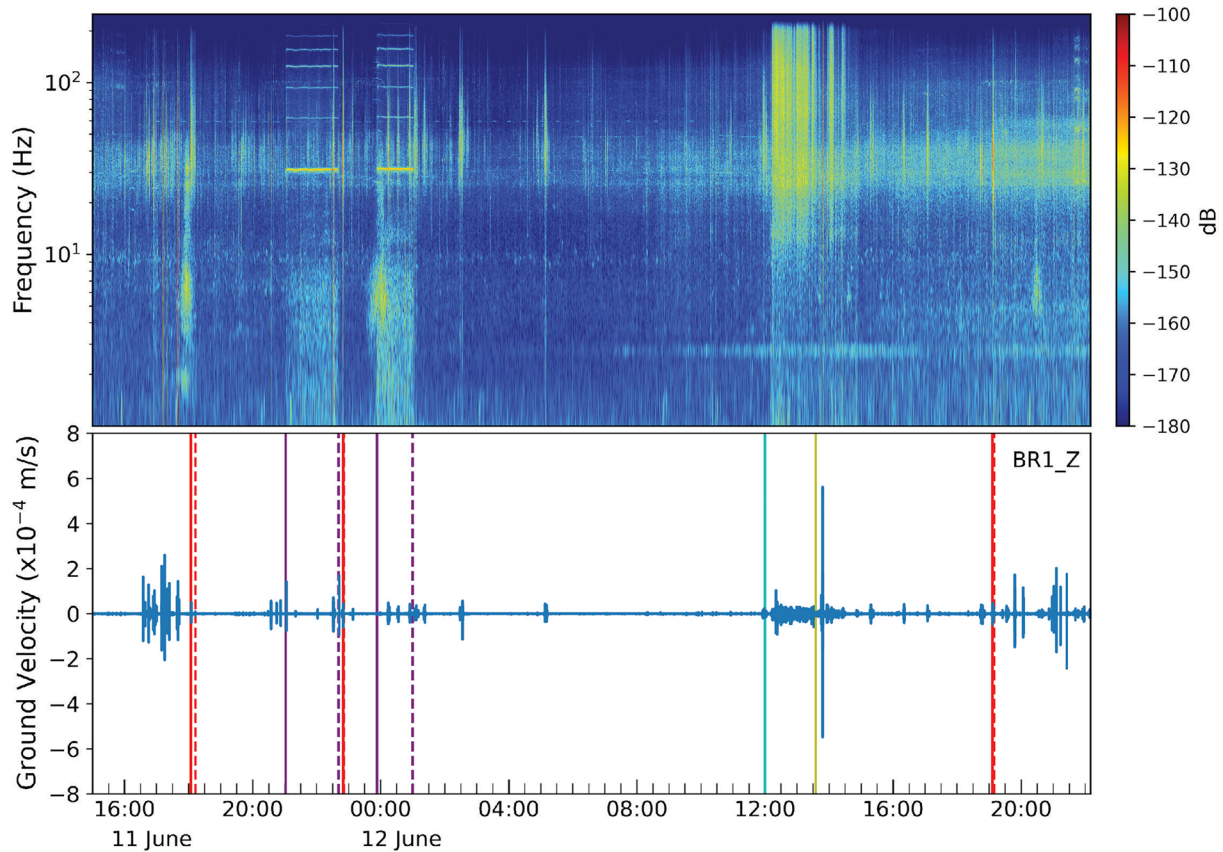


Figure 2. Full experiment seismic data from station BR1 (vertical component, other components, and stations shown in Figures S2–S13 in Supporting Information S1). Spectrogram (top) indicates seismic power in dB, relative to $1 \text{ (m/s)}^2/\text{Hz}$, based on ground velocity waveform data (bottom). Lines on waveform indicate key time periods during full deployment period (red— injection Experiments 1, 2, and 3; purple—pumping water to refill pool; cyan—start of rain event; green—start of flow at overflow spring). Solid vertical lines indicate start of activity, and dashed vertical lines indicate end of activity. The duration of injection Experiments 2 and 3 is very short so those solid and vertical lines almost overlap in the scale of the figure.

We also used F-K analysis to identify direction and slowness of primary seismic energy sources again using standard array analysis workflows in the ObsPy array processing package (Beyreuther et al., 2010). We used the vertical velocity components of all stations with time windows and bandpass filters determined as appropriate for the signal of interest and described in the relevant Section 4. Parameters for the array processing include $\pm 3 \text{ s/km}$ x -slowness and y -slowness limits with 0.02 s/km slowness steps, sliding window length of 1.0 s , window step fraction of 0.05 s , and no applied prewhitening. We compute total beam power in the defined windows from the covariance matrix of all array stations (e.g., Anthony et al., 2020; Beyreuther et al., 2010). As a result, we have a time series of absolute power, relative power (sum of the power at all stations normalized by the trace of the covariance matrix, providing a measure of how coherent the signals are), slowness (inverse of apparent horizontal velocity), and back azimuth (angle between north and the incoming seismic wave). We find the back azimuth and slowness where the relative power is at a maximum to report the direction to the source location of the coherent seismic signal.

4. Results

The seismometers captured a range of ground motion signals from several defined sources such as water flow during the injection experiments and pump-generated noise during periods of pool refilling, and signals associated with the rain and natural recharge event (Figures 2 and S2–S13 in Supporting Information S1). Two distant earthquakes with magnitude >5 occurred during the limited experiment duration; we used filtered signals from the largest of these earthquakes (2016-06-12T17:11:36.630 magnitude 5.3 earthquake in Russia $\sim 76^\circ$ epicentral distance, seismicity catalog from USGS, www.earthquake.usgs.gov, last accessed 22 June 2022) to confirm

seismic station timing and polarity. Based on visual scanning of time series amplitudes at each station, the largest amplitudes of the entire monitoring period occurred during the time period after flow initiation of the overflow spring from the natural recharge event at most of our seismometers. We describe here several sources of seismic energy, including noise or nonrelevant signals so that we can focus on signals associated with flow processes from both the injection experiments and the natural rain-driven recharge event.

4.1. Anthropogenic Noise

Human-caused seismic noise is readily apparent in our seismic data (Figure 2), but we have written records of many of these human activities so we can characterize this noise. One prominent signal apparent in the spectrogram is energy in monochromatic frequency bands over several hours; this is associated with the generator-powered pump used to refill the pools following injection Experiments 1 and 2. The primary band for this noise source is at 30 Hz, with secondary peaks at 60, 90, 120, 150, and 180 Hz. The spectral signal for this pump shows very clear start and end times that correspond with field notes associated with the experiment, so we are confident in the origin of these prominent signals and avoid interpreting other signals during these pumping periods.

Other waveform signals with large amplitudes are related to field teams working on the installation of other seismic and hydrologic instrumentation and/or farm animals moving around the on-site barn. Signals associated with field installations tend to be short duration signals on only specific stations, and we have field notes outlining the animal times during daylight hours. During the time of and immediately after the injection experiments, all on-site field activity ceased (for ~15–30 min) to minimize the human-generated noise on any flow signal. During the natural recharge event, field crews were on-site only after 13:13 UTC, and heavy rain kept the field teams in a nearby shelter away from the stations. Our estimate of the overflow initiation (between 13:13 and 13:40 UTC) comes from staggered visuals at the site, with a more specific time of 13:32–13:35 UTC based on the large increase in the measured discharge at the spring.

Another prominent anthropogenic noise source comes from nearby transportation routes. An active Class 1 major Canadian Pacific railroad line is present ~2.2 km north of our field site. In other studies, frequency content of train noise sources is dominated by Rayleigh wave energy of frequencies <~10–15 Hz (Quiros et al., 2016). Although we do not have published train schedules indicating the time of trains passing on the nearby line, we have on-site field notes of a train on day 11 June at ~17:50 UTC. In this case, we see a band of higher power between 3 and 8 Hz beginning 17:46 UTC, ending ~18:05 UTC (Figure S14 in Supporting Information S1). We observe a signal of similar duration and frequency while we were using the pump to fill the pool for the third injection experiment (11 June ~23:42–12 June 00:09 UTC).

4.2. Injection Experiments

The three injection experiments occurred with variable release rates or under different hydrologic conditions and produced different seismic signatures. The first two injection experiments on 11 June occurred with dry conditions at the overflow spring, and the final one on 12 June occurred after the overflow spring became activated; water was already flowing along the surface following the rain event, with no water entering the subsurface cavity based on direct observation. Seismic signals associated with these injection experiments are primarily observed at stations closest to the injection location (BR1, BR2, BR5, BR9, BR12), as shown in the time series (Figures 2 and S2–S13 in Supporting Information S1) and by the PSD computed for each injection experiment (Figures 3 and 4, time periods used for PSD calculation included in Table S1 in Supporting Information S1).

Both of the first two water injections caused minimal change in the ~100 L/s background spring discharge, but they did produce dye, dissolved salt, and water temperature changes. The dissolved salt concentration reached a peak at 17.4 and 8.1 min, respectively, for the first and second water injections, where a smaller peak and breakthrough curve during the second injection resulted from a faster water injection rate and residual salt in the system since no salt was added for the second injection. Most of the salt used in the first injection was recovered just downstream of the perennial springs within hours, and a majority of this salt was recovered within the first hour, indicating fast conduit flow below our seismic network.

The PSDs for each seismic component at a given station are similar (Figure 3), so we focus on the vertical component for the remaining discussion. At station BR1, located ~4.7 m from the pool location, each injection

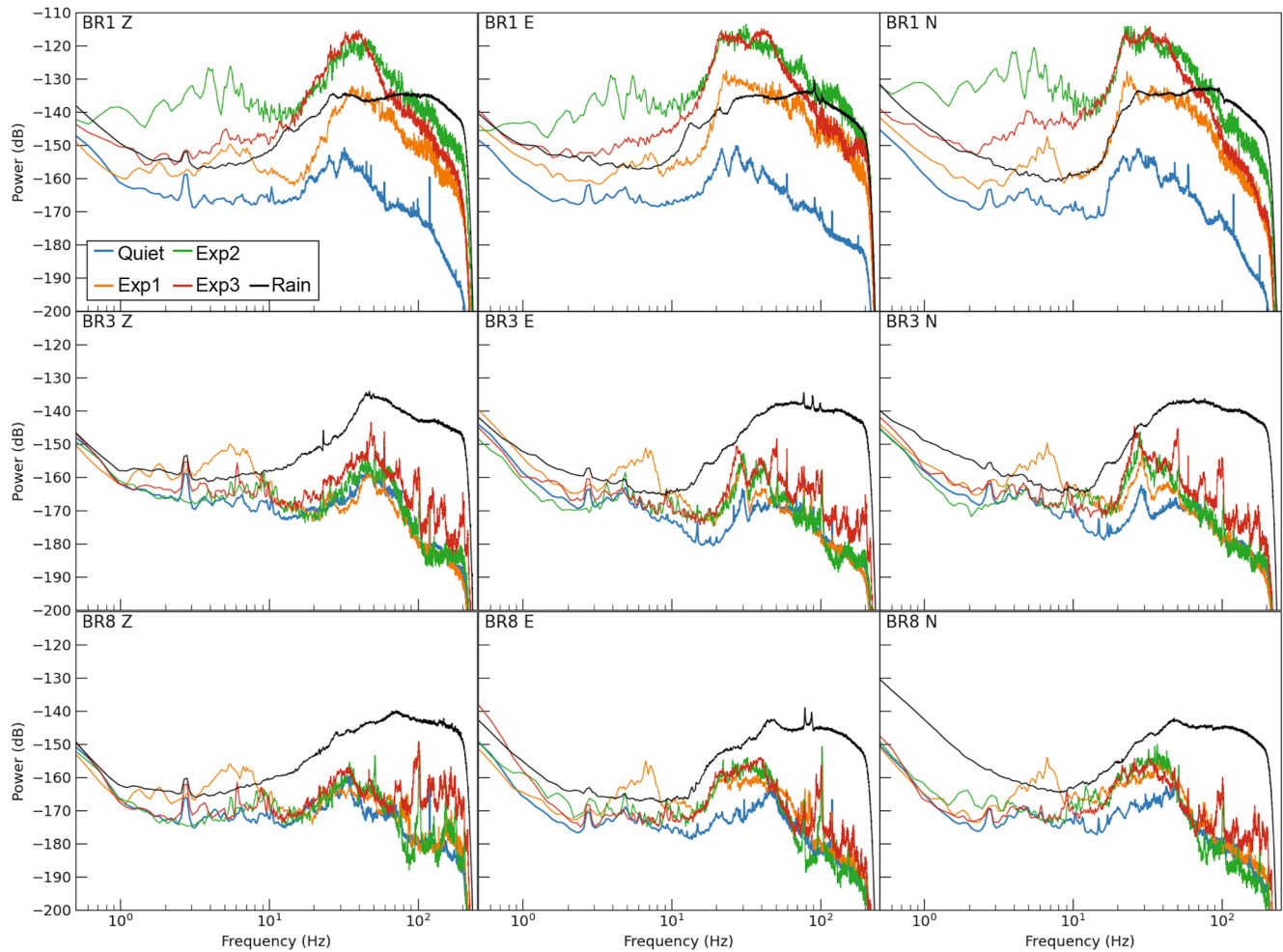


Figure 3. Power spectral density (PSD) for the key activities recorded for all components (Z = vertical, E = east, N = north) of three representative stations (BR1, BR3, BR8). Times used for PSD calculation are listed in Table S1 in Supporting Information S1. Quiet represents station background noise, using an hour-long data window during local nighttime hours (12 June 07:20–08:20 UTC, 02:20–03:20 a.m. local CDT) without background earthquakes or field site activity. Power is in dB, relative to $1 \text{ (m/s)}^2/\text{Hz}$.

experiment has power above the background noise at all frequencies $>1 \text{ Hz}$. Injection Experiments 2 and 3 had the fastest injection times; these also have the highest power of the three injection experiments over all frequencies $>1 \text{ Hz}$, with the largest increase in power (and very similar PSD overall) between ~ 20 and 70 Hz . Seismograms filtered between 20 and 75 Hz for Experiment 2 also contain some coherent peaks across the stations. Power is also elevated in the ~ 2 – 8 Hz band, largest for Experiment 2. For stations BR3 (39 m from pool) and BR8 (48 m), the PSD for each injection experiment is very similar to the background noise quiet period, with the exception of elevated power in the 3–8 Hz frequency range for Experiment 1 in all three components. We do not interpret this elevated low frequency power because of the train signal that overlaps in this time period.

Comparing PSDs for all injection experiments relative to the background quiet period (difference in power dB, Figures 4a–4c) highlights specific frequency bands to compare to hydrologic signals. For the injection experiments, the stations closest to the pool location have the largest increase in power over background noise. During the first injection experiment, most stations have an increase of 10–20 dB in the $<10 \text{ Hz}$ frequency range, although this also overlaps with the train signal contamination. Closest station BR1 has larger (~ 15 – 30 dB) power increases throughout much of the recorded frequency range, but stations within 25–30 m (pink lines, Figure 4) have smaller power increases ($<10 \text{ dB}$) largely between ~ 30 and 60 Hz and above 125 Hz (Figure 4a). For the second injection experiment, a similar pattern exists with the highest power above background observed at the closest stations, with peaks in power in the 2–8 Hz range for the closest stations, as well as other ranges of

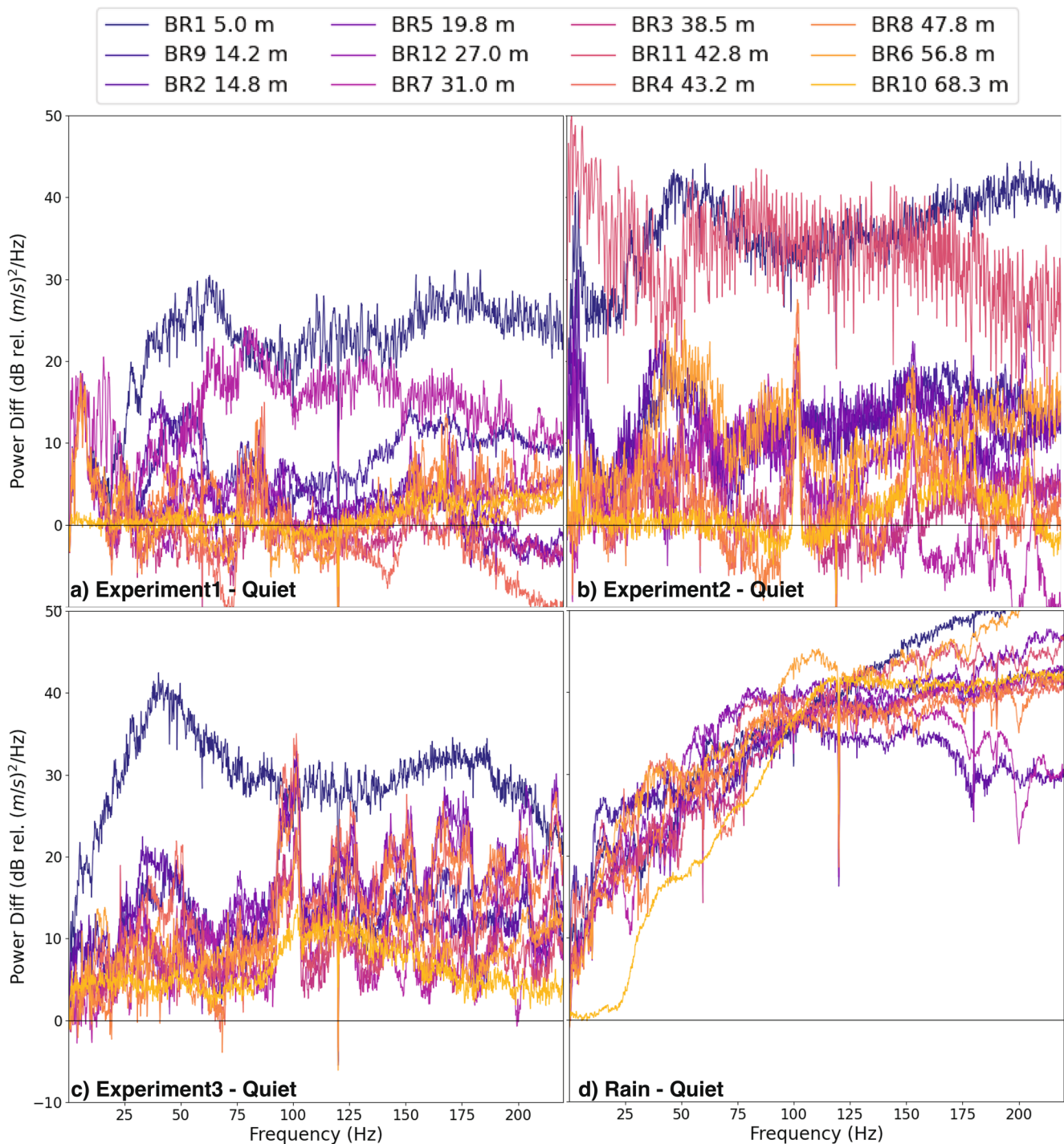


Figure 4. Difference in dB ($10\log_{10}\text{PSD}_{\text{Signal}} - 10\log_{10}\text{PSD}_{\text{Quiet}}$) between time period of interest and the background quiet period (12 June, 07:20–08:20 UTC) for vertical component of each station, colored by distance between station and pool location (5–68 m). (a–c) Results for injection experiments. Stations closest to the pool location for the injection experiments have increased power relative to the background noise of up to 30–40 dB, and the power difference decreases within increasing distance, in some cases having power lower than representative background noise. BR11 signal window for Experiment 2 contains 2 s of long period instrument noise, raising the power for that station in panel (b). (d) Rain signal has increased power above background noise at all frequencies with no consistent pattern with distance from the pool location.

higher power at ~ 20 –70 and > 150 Hz (Figure 4b). During the third and final injection experiment (Figure 4c), we find that the stations closest to the injection point again have the largest power increase above background, although in this case most stations have elevated power over the broad range of frequencies instead of peaks at

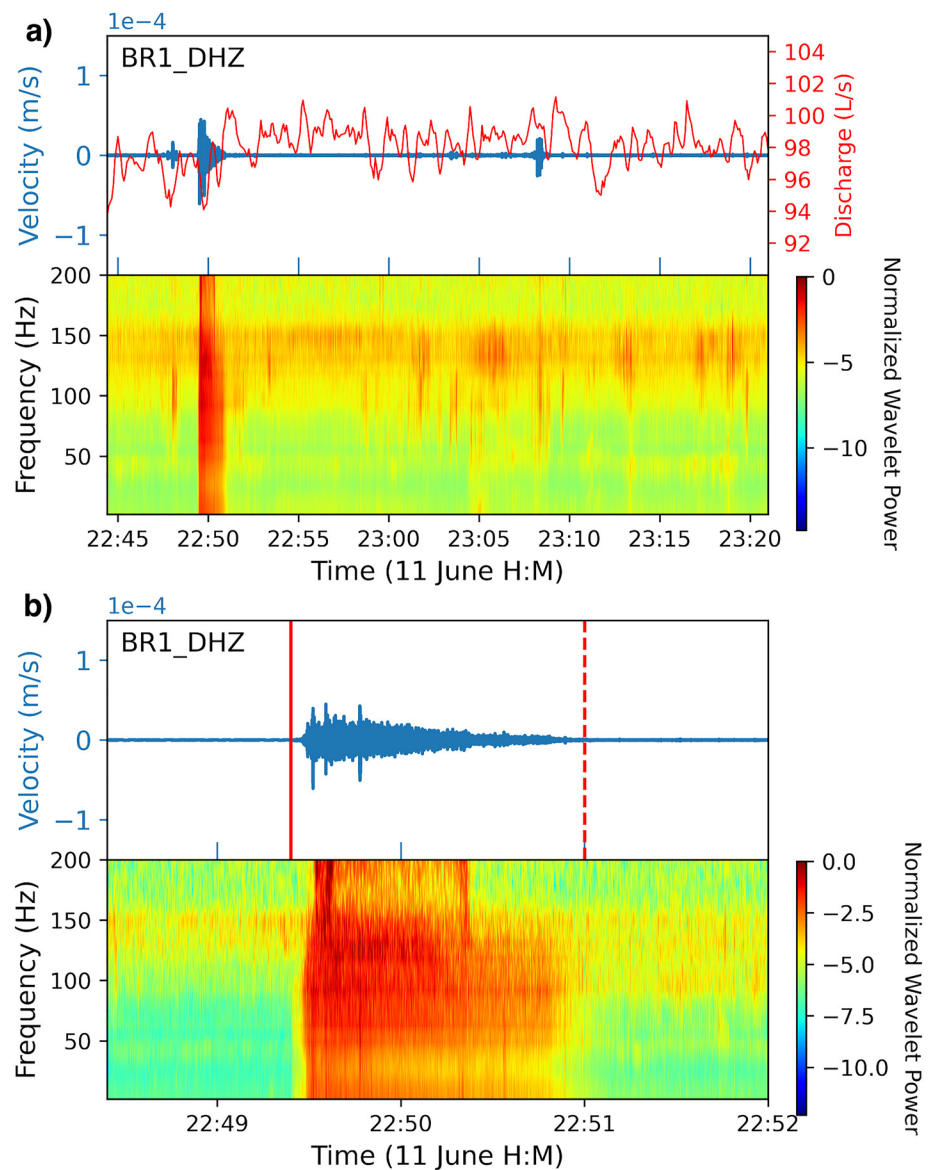


Figure 5. Seismic and hydrologic data for the second injection experiment. (a) Top: seismogram (blue) and measured and smoothed discharge record (red) for 5 min prior to the start of the injection and 30 min following the end of water injection. The discharge data were recorded just upstream of the weir by the Van Essen CTD-Diver. Scalogram (the CWT equivalent to Fourier transform spectrogram, bottom) shows increase in power during the active injection period with limited signal above background levels in the 30 min following the experiment. Normalized wavelet power describes CWT amplitudes, similar to dB as shown in spectrogram, with red colors indicating more energy than green/blue colors. (b) Seismogram (top) and scalogram (bottom) focused on the few minutes of active injection (indicated by red vertical lines (solid start, dashed end) on seismogram, window includes 1 min before and after active injection).

2–8 and ~20–60 Hz. BR1 has the largest power increase over the full frequency range, up to 40 dB at 40–45 Hz, whereas the other stations have a consistent ~5–20 dB increase over the full range.

Comparison with the hydrologic data and video collected during these injection experiments suggests that seismic signals are likely from the act of pouring water from the pool and from the falling water impacting the rock at the base of the slope as water entered the overflow spring. The second injection experiment timing was shortest (total time of water injection was 1 min 36 s), best representing a rapid influx of water into the overflow spring and conduit system. However, even in this rapid injection scenario, there was only a <5 L/s increase in measured discharge in the 30 min following the experiment (Figure 5). A detailed comparison between video of the active

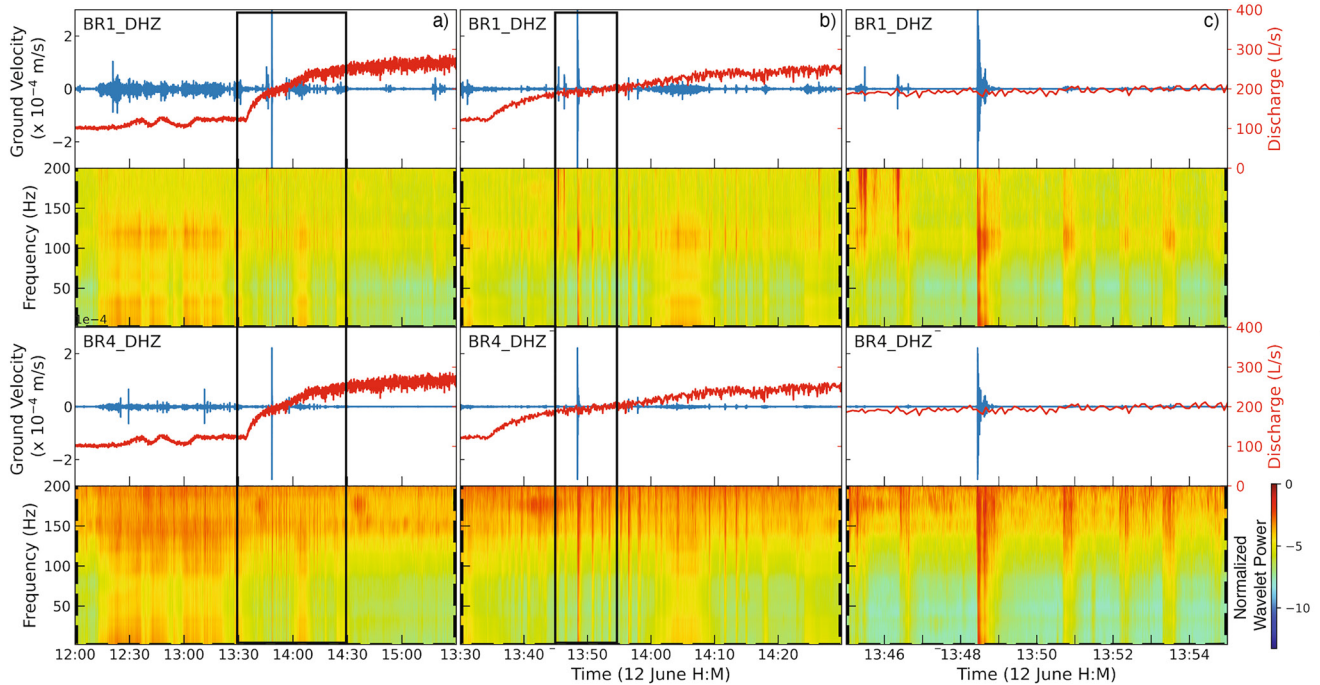


Figure 6. Seismic and discharge data for the natural recharge period on representative stations BR1 and BR4. The discharge data were recorded just upstream of the weir by the Van Essen CTD-Diver. (a) Full time period of natural recharge event on 12 June 2016. Upper panel shows vertical component ground velocity seismogram (blue) with measured discharge (red), and bottom panel shows continuous wavelet transform scalogram for the seismic data in upper panel. Black box marks time period displayed in (b). (b) Time period showing largest change in discharge. Both stations have short duration broadband pulses of higher power as the discharge begins to increase. Black box marks time period displayed in (c). (c) Focused 10 min surrounding the largest amplitude seismic signal recorded during the experiment. The largest amplitude ground motions correspond to the highest wavelet power in the broadband peak in the scalogram. Scalogram indicates several additional pulses of high wavelet power following this large peak, all with similar spectral characteristics to the earlier pulses.

injection, the ground velocity seismogram, spectrogram, and discharge record suggests that the elevated seismic power occurs only during the active injection, and seismic power largely returns to the background levels following the active injection time.

4.3. Natural Recharge Event

In contrast to the seismic and hydrologic response of the injection experiments with relatively small water inputs, the large rain event that occurred on the final day of our experiment caused much larger increases in discharge (~200 L/s) and seismic responses (~1 μm ground displacement). Intense rainfall occurred at the site for ~70 min, as noted by increased broadband noise (Figures 4 and 6) observed in the seismic data at all stations and consistent with precipitation data from the nearby weather stations. Another period of increased seismic noise occurs between 14:00 and 14:10 UTC, which we also interpret as rain. During the first period of intense rainfall (~12:15–13:25 UTC), minor increases (a few 10s of L/s) in discharge are also observed. The largest increase in discharge, from 120 to ~225 L/s, occurs between ~13:35 and 14:00 UTC. This is ~10 min after a period of intense rainfall, which we inferred from increased broadband seismic noise during the period of rain and corresponds to the time when hydrologic conditions changed to include overland flow along the path between the overflow spring and the discharge measuring station (overflow run in Figure 1). Flow along the overflow run was observed for the remainder of the seismic experiment.

Seismic data from this natural recharge period show several changes in amplitude as well as frequency content. During the time period between 13:30 and 13:45 UTC (Figure 6b), we observe several short duration peaks (few seconds) of seismic power over a wide frequency range as the discharge begins to increase. Between ~13:45 and 13:50 UTC, we see the largest amplitude ground motions coherently recorded at all stations over the entire 2-day experiment outside of known field activity noise generated close to particular stations. Within this window, large amplitude signals at 13:45 UTC contain most energy at frequencies >100 Hz, but the largest amplitude ground

motion at 13:48 UTC contains strong energy at frequencies over a broader band, focused for some stations at 20–50 Hz and others shifted to higher frequencies (50–100 Hz, Figures 6 and 7).

Within the large amplitude pulse, several discrete pulses can be identified in the waveforms, both in the velocity seismograms or those integrated to ground displacement (Figure 7b). The first of these pulses arrive earliest at the northernmost stations in the array (BR10 and BR6), arriving later to the southern part of the array. Later pulses in the sequence do not appear to follow a similar moveout nor have the same waveform shape, suggesting a different location generating these seismic pulses. The time between pulses also varies within the sequence. At least 10 individual pulses can be identified in the displacement waveforms within the first 6 s following the large peak; however, many more are present both before and after these largest amplitude peaks based on similar streaks apparent in the scalograms as the discharge increased and flow initiated along the overflow run. Frequency content of these peaks varies between stations. For this time window of the largest amplitude signal, stations BR1, BR12, B8, and BR5 have PSD peaks at 30–35 Hz, stations BR7 and BR11 have peaks at 40–45 Hz, BR2, BR3, and BR4 have peaks between 50 and 60 Hz, and BR10 and BR6 have peaks at 65–70 Hz (Figure 7).

4.4. Array Analysis

Because we do not have a detailed model of the seismic velocity structure in the local area, more traditional attempts at locating the sources of these large amplitude natural recharge pulses based on first arrival times yield location estimates with very large (50–100+ m) uncertainties. Therefore, we use F-K analysis with the seismic array data to determine the back azimuth and slowness (inverse of the apparent horizontal velocity) for the dominant energy in these seismic pulses relative to our array (using station BR7 as the array center). The slowness and summed relative power are displayed in a polar representation (Figures 8–10) to indicate the back azimuth of the dominant energy (i.e., highest summed relative power) within the time window of interest and plotted with respect to time to correlate to the peaks on the seismograms.

As a test of the F-K analysis to estimate source regions of known activities, we use signals from the second, rapid injection experiment and compare with the video recording of the experiment indicating location and timing of the injection. During the first 20 s as the water flowed down the slope between the pool location and the overflow spring, water impacted bare rock nearly vertically at the base of the slope. Following those initial seconds, water ponded at the overflow spring to form a layer between the flowing water and the rocks at the base of the slope. During this time window, we find large amplitude, lower frequency ground motions at the stations closest to the spring (BR1, BR2, BR5, BR9, BR12, Figure 8a). We apply F-K analysis on the signals in that 20-s period, here filtered between 1 and 8 Hz because this signal is dominated by low frequencies. We find the highest relative power at a back azimuth, or direction to the source, of 250° from north and 0.77 km/s apparent velocity (slowness of 1.3 s/km). This back azimuth direction is WSW of the array center, consistent with a location at the overflow spring where water impacted the ground.

We also incorporate seismic data encompassing the entire duration of the second injection experiment but filtered at higher frequencies (25–70 Hz). This frequency range was selected because some coherent peaks are visible in the seismograms filtered in that range (Figure 9) and the PSDs suggest an increase in power at these frequencies (Figure 4b). The higher frequency analysis indicates seismic power more distributed over the range of back azimuth, but the highest summed relative power originated south of the array (back azimuth of 190°) with an 0.52 km/s apparent velocity (slowness of 1.9 s/km, Figure 9). Although this analysis does not provide a specific source location for these signals, a different back azimuth for the source is clear. We are confident in the source location and activity generating the low frequency signal based on on-site visuals and the video recording of the experiment; this energy did originate at the overflow spring at the surface, which is west of the array center (Figure 8). The southern source direction for the high frequency signal suggests a different source location (Figure 9).

Injection Experiments 1 and 3 occur with different experimental conditions that affect the F-K analysis results. For the slow injection Experiment 1, both low frequency energy (1–8 Hz) and higher frequency (25–70 Hz) are largely sourced from south of the array, although the higher frequency band also includes a source from the northeast (Figure S15 in Supporting Information S1). For Experiment 3, no water entered the conduit at the overflow spring, but instead flowed over land from the pool to the northern spring. Analysis of both low frequency (1–8 Hz) and higher frequency (25–70 Hz) signals during Experiment 3 suggests higher relative power coming

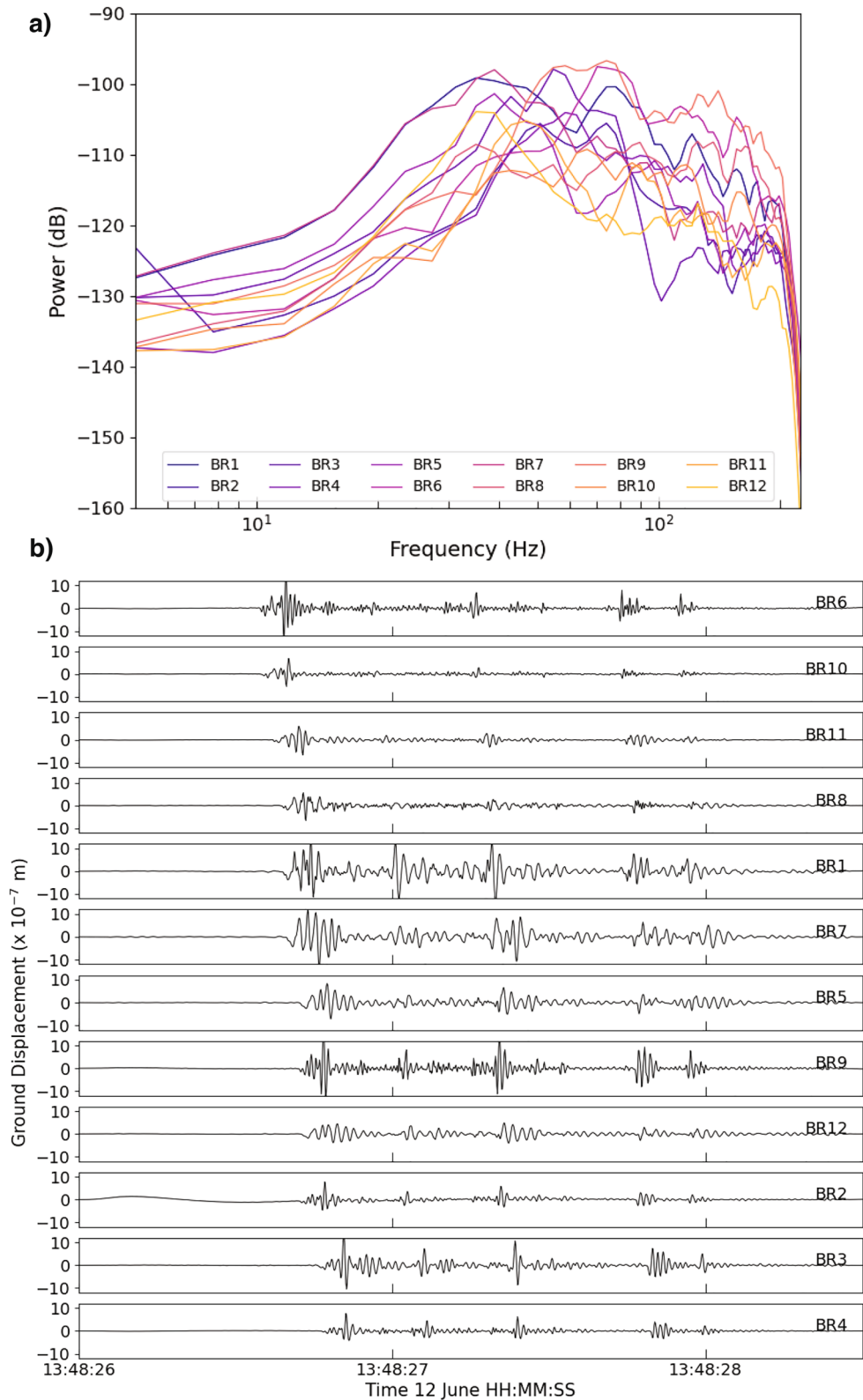


Figure 7. Spectral properties and waveforms of the largest amplitude signal during the natural recharge event. (a) Power spectral density (in dB relative to 1 m²/Hz) for the largest amplitude seismic signal using vertical component data for all stations shown in (b). (b) Ground displacement, determined by integration of the velocity seismograms, for 2.5 s around the largest amplitude signal. Several discrete pulses are present within this signal, with first arrivals coming to stations in the northern portion of the array (BR6 and BR10).

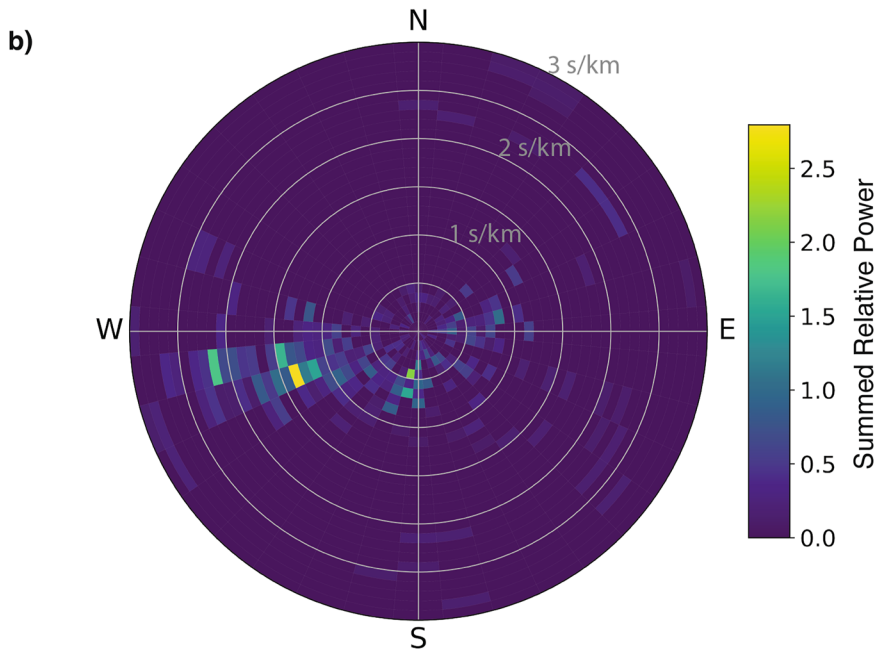
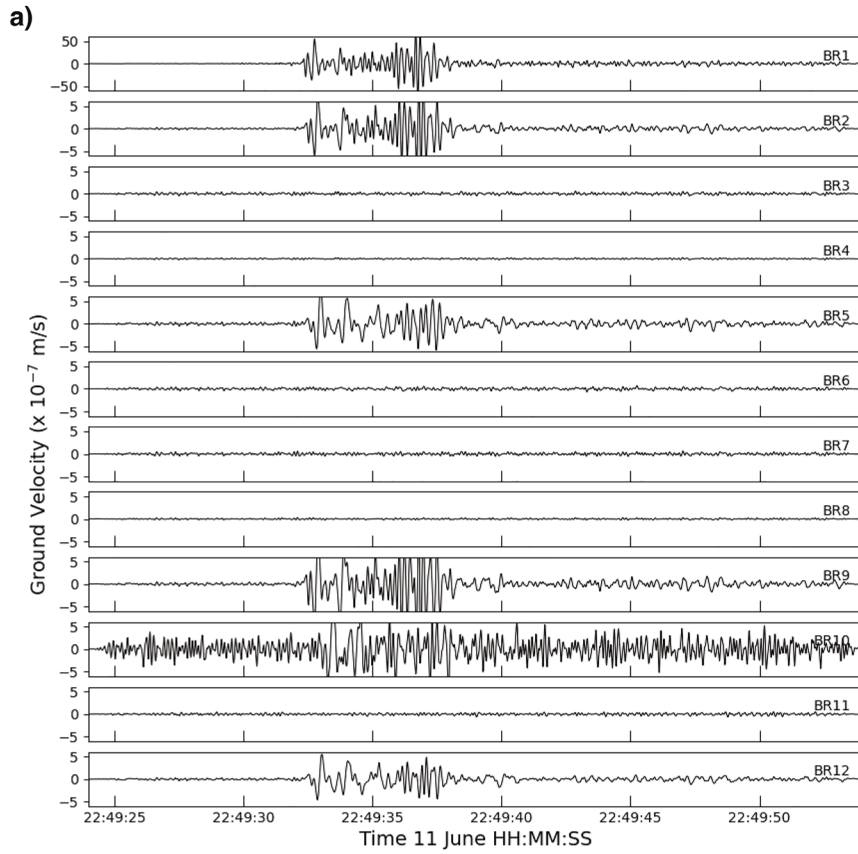


Figure 8.

from the west-southwest (Figure S15 in Supporting Information S1), in the direction of the surface pool and similar to the low frequency signals during the initial seconds of injection Experiment 2.

We apply the same analysis to a 20-s long seismogram window containing the largest ground motion amplitudes observed during the natural recharge event, filtered to 30–70 Hz to include the highest power in these peaks based on the PSDs (Figure 7). In this case, we find two primary locations, one to the northwest of the array, and one to the south (Figure 10). The change in back azimuth occurs over this 20-s long window, with the northwestern back azimuths corresponding to the first and largest amplitude peak, followed by a transition toward the southern back azimuths later in the sequence. A northwestern source for the earliest large pulse(s) is consistent with the observation of the phase timing on the seismograms, with the earliest pulses in the sequence arriving first at the northern stations BR10 and BR6 (Figure 7). The southern source (back azimuths 170°–200°) for energy later in the sequence is similar to the high frequency results for the second injection experiment (Figure 9), although with a slower apparent velocity of 0.48 km/s (slowness of 2.1 s/km). There are additional, smaller amplitude pulses that occur during the earlier period of increasing discharge between UTC 13:35 and 13:46 (Figure 6). Using the same filters and analysis, we find similar southern back azimuths (190°–200°) for these earlier pulses (Figures S17b and S17c in Supporting Information S1). In contrast, results from a representative 4-min period (UTC 12:30–12:34) during the initial period of rain without any changes in measured discharge suggests more heterogeneous back azimuths, as might be expected for heavy rain occurring everywhere at the site (Figure S17a in Supporting Information S1).

5. Discussion

The goal of our project was to document seismic signals associated with changing flow conditions within a karst aquifer system. The project included controlled injection experiments from surface pool injections as well as a fortuitous rain event that increased spring discharge rates nearly three times above background rates. Each generate seismic responses, and we discuss these responses below, organized by either injection experiment or rain event.

5.1. Injection Experiments

The salt recovery indicated that the injected water quickly passed from the overflow spring to the perennial springs via one or more conduits below our seismic network, but the amount of water injected into the system by dumping from the ~13,000 L surface pool did not produce a significant increase in the amount of discharge within the conduit. Thus, seismic signals associated with subsurface flow from our injection experiments are likely difficult to observe. This is in contrast to glacial studies that find low frequency (1–10 Hz) tremor signals correlated with large changes in subglacial discharge within conduits (e.g., Bartholomaeus et al., 2015). In our experiments, we observe seismic signals associated with the act of pouring the water from the pool. One type of seismic signal is low frequency (1–8 Hz) energy associated with water impacting the rocks at the opening of the overflow spring at the base of the slope when the water volumes hitting this area are large (rapid injection of injection Experiment 2). The F-K analysis suggests a west-southwestern source (back azimuth of 250°) of this energy (Figure 8), which is in the direction of the overflow spring location relative to the center of the array (Figure 1). It is difficult to interpret whether the low frequency signal exists for the first injection experiment because of the timing of a train (based on on-site documentation and seismic signature, Figure S14 in Supporting Information S1) that passed prior to and during the experiment. However, it is reasonable to conclude that this first injection experiment did not produce this low frequency signal because the time period of injection was much longer, leading to less water volume impacting the overflow spring at a given time relative to the rate of the second experiment. A similar low frequency signal may also be apparent during the early stages of the third injection experiment which had a similar fast pouring rate as Experiment 2. F-K analysis of this experiment suggests energy with a source west-southwest of the array center over a range of frequencies, consistent with the location of the overflow spring (Figure S16 in Supporting Information S1).

Figure 8. Seismograms of injection Experiment 2 with F-K analysis results. (a) Ground motion seismograms windowed for the first 30 s and filtered between 1 and 8 Hz to highlight the low frequency signals associated with water hitting bare rock in the initial stage of the experiment. Note the different y-axis limits for station BR1, but all other panels are plotted at the same y-scale. (b) Summed relative power (unitless) associated with all possible back azimuths and slowness (slowness indicated by labeled gray circles, 0 s/km in center to 3 s/km at outside edge of circle). See Figure 1 for array geometry, station BR7 defined as array center. Largest relative power occurs at 250° back azimuth, relative to north and 1.3 s/km slowness (0.77 km/s apparent velocity).

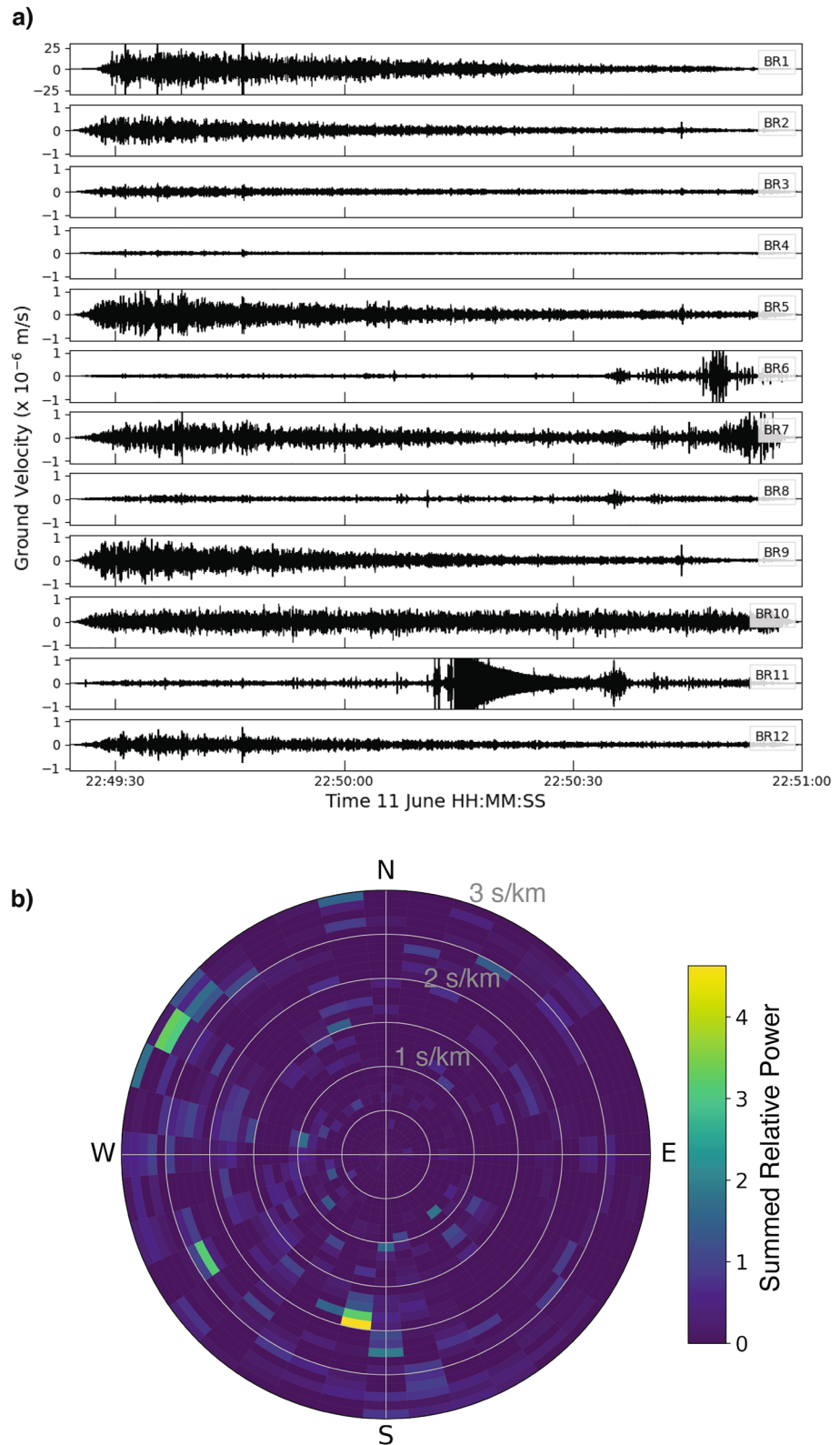


Figure 9. Filtered (25–70 Hz) seismograms of the entire duration of the second injection experiment and polar representation of summed relative power with respect to back azimuth and slowness. (a) Ground motion seismograms (note different y-axis limits for station BR1, all other panels plotted at same y-scale) and (b) summed relative power (unitless) associated with all possible back azimuths and slowness (up to 3 s/km). Largest summed relative power occurs at 190° back azimuth and 1.9 s/km slowness.

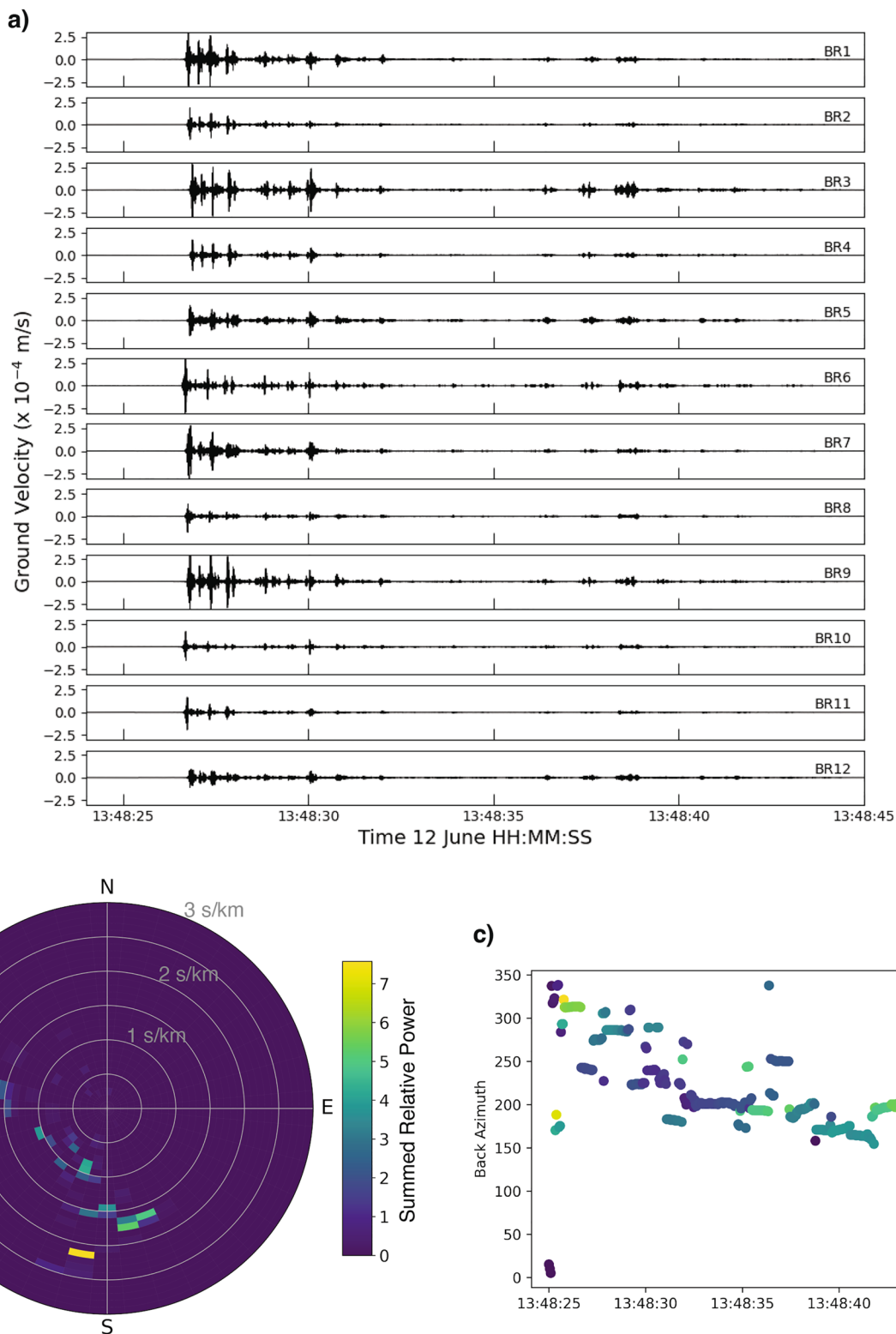


Figure 10. Filtered (30–70 Hz) waveform and estimated back azimuth and slowness for the time window around the largest waveform peaks during the natural recharge event. (a) Seismic data window for 21 s includes several sequences of discrete pulses. (b) F-K analysis results suggest peak relative power from southerly back azimuths (170°–200°) with variable slowness, and one other area of high relative power to the northwest of the array. (c) Back azimuth as a function of time, circles colored by slowness. The northwestern energy occurs early in the window for the largest amplitude pulse, followed by a transition to energy dominantly from the southern back azimuths within the first few seconds.

Another type of signal apparent during the second injection experiment included coherent seismic pulses at much higher frequencies (25–70 Hz) that occurred ~22 s after the start of the injection. These signals are higher frequency than typically described in the subglacial seismic studies (e.g., Bartholomaeus et al., 2015; Vore et al., 2019), possibly reflecting a different source mechanism or simply that the signal is less attenuated because of the close proximity to our stations (e.g., Gimbert et al., 2014). F-K analysis of bandpass filtered (25–70 Hz) seismograms during the full extent of the second experiment suggests a source location in the south of the array. This source location is different from the orientation determined for the low frequency signals at the start of the experiment that we attribute to water hitting the rocks at the entrance to the overflow spring. Based on mapping of the conduit, a sump is located east-southeast of the pool location, at which there is a large change in conduit orientation, from a northwest-southeast oriented conduit to a southwest-northeast trend (Figure 1). We suggest rapid interaction of the water with this sump and change in conduit orientation leads to the generation of these higher frequency seismic pulses.

5.2. Rain Event

The largest amplitude seismic signals during the study occurred during the rising limb of the hydrograph of the natural flood event, although not during the initial period of most rapid rise. There are several aspects of the observed sequence of events that can help constrain potential source mechanisms of the seismic energy. Within a ~6-s window starting at the largest waveform amplitudes, there are several shorter duration pulses, typically <0.25 s. The first four pulses occur with a relatively regular spacing of about 0.3 s, but this spacing becomes less consistent later in the sequence (Figure 7).

The broadband rain signal dominates during the active rain period, similar to that observed in other environmental seismology studies (e.g., Bakker et al., 2022), so it is difficult to determine if similar discrete pulses exist earlier in the rain event. We are able to observe discrete pulses as discharge begins to rapidly increase and surface flow begins along the overflow spring run. Because of this timing, it is reasonable to conclude that these seismic pulses are related to the changes within the conduit system as it filled. Estimates of the source locations based on the F-K analysis of the high frequency signals highlight two different regions for this energy. The earliest pulses appear to be generated to the northwest of the seismic array, whereas later pulses appear to originate south of the array (Figure 10).

A southern source direction for most of the high frequency signals resulting from the rain filling the conduit is similar to the source direction estimated for the later high frequency signals associated with the second injection experiment. Apparent horizontal velocity and slowness of the energy during both of these events are also similar. Because of these consistent seismic attributes, we assume a similar mechanism leading to this high frequency energy during these recharge events.

5.3. Possible Mechanisms

There are several different mechanisms that could be physically plausible as sources for the range of seismic pulses observed during our full experiment encompassing injection and rain: (a) release of air pockets that have been compressed as a result of a flooding conduit, similar to what is possible in analogous stormwater drainage pipes (e.g., Wright et al., 2017), (b) arrest of a flood bore by a constriction within the conduit, and (c) rockfall or brief movement of large clasts (e.g., Burtin et al., 2016) within the conduit. During our experiment, multiple mechanisms may have been at work because of the different energy source locations. The largest amplitude signals originate northwest of the array, later in the rain event following the time of rapid increases in discharge. This largest amplitude signal could be the result of a rockfall or large clast movement in the northwest. However, the majority of the pulsed seismic energy during periods of water level increase in the conduit, both during injection Experiment 2 and during the rain event, was generated from south of our array, an area where significant geometric changes exist, with both the sump location and changes in the conduit orientation. Those geometric changes may be important especially for air pocket release and flood bore arrest mechanisms. Theoretical modeling for these different mechanisms will be useful to distinguish between the possibilities, but out of the scope of this manuscript detailing the signal observations. The modeling effort is the subject of an ongoing study.

These mechanisms may not be valid for the seismic pulses recorded during the first and third injection experiments because of the very different conditions associated with those injections. The first injection experiment

occurred over a much longer time period (nearly 9 min instead of 1.5 min). Given that slow injection of water, it is likely that the water introduced into the conduit system is not rapid enough to trigger the mechanisms we list above. Water did not enter the conduit system during the final injection experiment because of the existing flow at the overflow spring and along the overflow spring run; our analysis suggests a west-southwest location for the energy consistent with the surface pool location. Thus, any of the mechanisms that occur within the conduit would not be triggered by this injection.

6. Conclusions

Our karst flow experiment, which involved a temporary deployment of various seismic and hydrologic sensors, captured signals from both our injection experiments, and fortuitously, a natural recharge event associated with a large rainstorm. The water injection during the first two experiments generated negligible discharge increases at the perennial spring, but other tracers in the pool water indicated a direct connection between the overflow spring used as the injection point and the perennial spring. The second injection experiment produced low frequency seismic signals that we interpret as resulting from initial water impacts on the rock at the overflow spring and higher frequency signals as the initial slug of water from the pool reached the sump location in the conduit.

The natural recharge event generated the largest coherent seismic ground motions and caused the overflow spring to start flowing and total discharge of the system to increase threefold. The largest amplitude ground motions occurred as discharge increased, producing a series of pulses over several seconds with peak frequencies of ~30–70 Hz. Based on array processing of the seismic data, it appears that at least two distinct sources in the study area, one to the northwest, and one to the south of the array, are important for generating these pulsed seismic signals. Relevant mechanisms that may have been responsible for these signals include the release of compressed air pockets with rising water levels, arrest of a flood bore by a conduit constriction, or a rockfall or large clast movement within the conduit, but additional modeling is needed to narrow down the possible mechanisms in this case.

The field of environmental seismology enables the monitoring and characterization of numerous earth surface processes. Even in the short time period of our field study, seismic signals were generated both during injection experiments as well as a natural recharge event, resulting from flow into a partially mapped karst conduit or cave. That these signals originated from conduits below the surface indicates that seismic monitoring provides a novel approach to remotely observe and characterize subsurface processes. Furthermore, while extensive maps are available for several caves throughout the world, new caves and passages are continually being discovered, and thus, our knowledge of preferential flow paths in the subsurface is far from complete. There are also other pathways that are too small to allow human entry. Consequently, seismic monitoring not only enables the capture of subsurface processes, but also the identification of source locations with potential applications that range from aquifer flow monitoring to the determination of contaminant pathways to sinkhole hazard maps.

Acknowledgments

We are grateful to Rio Diniakos, Emily Morton, Pina Miller, Noel Barstow, Jeffrey Green, Alex Rinehart, and Glenn Spinelli for their help in completing this field study and to Brian and Sara Halvorson for allowing us to complete this project on their property. A. Luhmann thanks Sridhar Anandakrishnan for a conversation that planted the seed for this research. This material was based upon work supported by the National Science Foundation under Grant 1850667. Seismic instruments were provided by the Incorporated Research Institutions for Seismology (IRIS) through the PASSCAL Instrument Center at New Mexico Tech. The facilities of the IRIS Consortium are supported by the National Science Foundation's Seismological Facilities for the Advancement of Geoscience (SAGE) Award under Cooperative Support Agreement EAR-1851048.

Data Availability Statement

The seismic data collected to monitor the karst aquifer in the study are available through the IRIS Data Management Center under the network code of XK: https://doi.org/10.7914/SN/XK_2016. Hydrologic data (Luhmann et al., 2023; atmospheric pressure, atmospheric temperature, voltage, electrical conductivity, temperature, level, discharge, and dissolved NaCl) are available through the HydroShare data repository: <http://www.hydroshare.org/resource/74a7fedb4f694ab6aafa3e6d6f47d129>.

References

- Almagro Vidal, C., Zaccarelli, L., Pintori, F., Bragato, P. L., & Serpelloni, E. (2021). Hydrological effects on seismic-noise monitoring in karstic media. *Geophysical Research Letters*, *48*, e2021GL093191. <https://doi.org/10.1029/2021GL093191>
- Anthony, R. E., Aster, R. C., Ryan, S., Rathburn, S., & Baker, M. G. (2018). Measuring Mountain river discharge using seismographs emplaced within the hyporheic zone. *Journal of Geophysical Research: Earth Surface*, *123*, 210–228. <https://doi.org/10.1002/2017JF004295>
- Anthony, R. E., Ringler, A. T., Wilson, D. C., Zebulun Maharrey, J., Gyure, G., Pepiot, A., et al. (2020). Installation and Performance of the Albuquerque Seismological Laboratory Small-Aperture Posthole Array. *Seismological Research Letters*, *91*, 2425–2437. <https://doi.org/10.1785/0220200080>
- Aso, N., Tsai, V. C., Schoof, C., Flowers, G. E., Whiteford, A., & Rada, C. (2017). Seismologically observed spatiotemporal drainage activity at Moulins. *Journal of Geophysical Research: Solid Earth*, *122*, 9095–9108. <https://doi.org/10.1002/2017JB014578>

- Aster, R. C., & Winberry, J. P. (2017). Glacial seismology. *Reports on Progress in Physics*, 80(12), 126801. <https://doi.org/10.1088/1361-6633/aa8473>
- Bakker, M., Legout, C., Gimbert, F., Nord, G., Boudevillain, B., & Freche, G. (2022). Seismic modelling and observations of rainfall. *Journal of Hydrology*, 610, 127812. <https://doi.org/10.1016/j.jhydrol.2022.127812>
- Barrière, J., Oth, A., Hostache, R., & Krein, A. (2015). Bed load transport monitoring using seismic observations in a low-gradient rural gravel bed stream. *Geophysical Research Letters*, 42, 2294–2301. <https://doi.org/10.1002/2015GL063630>
- Barry, J. D., Miller, T. P., Steenberg, J. R., Runkel, A. C., Kuehner, K. J., & Alexander, E. C., Jr. (2020). Combining high resolution spring monitoring, dye tracing, watershed analysis, and outcrop and borehole observations to characterize the Galena Karst, Southeast Minnesota, USA. In *NCKRI Symposium 8, 16th Sinkhole Conference*. <https://doi.org/10.5038/9781733375313.1012>
- Bartholomaus, T. C., Amundson, J. M., Walter, J. I., O'Neel, S., West, M. E., & Larsen, C. F. (2015). Subglacial discharge at tidewater glaciers revealed by seismic tremor. *Geophysical Research Letters*, 42, 6391–6398. <https://doi.org/10.1002/2015GL064590>
- Beyreuther, M., Barsch, R., Krischer, L., Megies, T., Behr, Y., & Wassermann, J. (2010). ObsPy: A Python toolbox for seismology. *Seismological Research Letters*, 81(3), 530–533. <https://doi.org/10.1785/gssrl.81.3.530>
- Bilek, S. (2016). Delineating preferential flow paths from recharge for water planning and management [Dataset]. International Federation of Digital Seismograph Networks. https://doi.org/10.7914/SN/XK_2016
- Birk, S., Wagner, T., & Mayaud, C. (2014). Threshold behavior of karst aquifers: The example of the Lurbach karst system (Austria). *Environmental Earth Sciences*, 72(5), 1349–1356. <https://doi.org/10.1007/s12665-014-3122-z>
- Budd, D. A., & Vacher, H. L. (2004). Matrix permeability of the confined Floridan aquifer, Florida, USA. *Hydrogeology Journal*, 12(5), 531–549. <https://doi.org/10.1007/s10040-004-0341-5>
- Burtin, A., Bollinger, L., Vergne, J., Cattin, R., & Nábělek, J. L. (2008). Spectral analysis of seismic noise induced by rivers: A new tool to monitor spatiotemporal changes in stream hydrodynamics. *Journal of Geophysical Research*, 113, B05301. <https://doi.org/10.1029/2007JB005034>
- Burtin, A., Cattin, R., Bollinger, L., Vergne, J., Steer, P., Robert, A., et al. (2011). Towards the hydrologic and bed load monitoring from high-frequency seismic noise in a braided river: The “torrent de St Pierre”, French Alps. *Journal of Hydrology*, 408(1–2), 43–53. <https://doi.org/10.1016/j.jhydrol.2011.07.014>
- Burtin, A., Hovius, N., & Turovski, J. M. (2016). Seismic monitoring of torrential and fluvial processes. *Earth Surface Dynamics*, 4(2), 285–307. <https://doi.org/10.5194/esurf-4-285-2016>
- Burtin, A., Vergne, J., Rivera, L., & Dubernet, P. (2010). Location of river-induced seismic signal from noise correlation functions: Location of river seismic signal. *Geophysical Journal International*, 182(3), 1161–1173. <https://doi.org/10.1111/j.1365-246X.2010.04701.x>
- Clements, T., & Denolle, M. A. (2018). Tracking groundwater levels using the ambient seismic field. *Geophysical Research Letters*, 45, 6459–6465. <https://doi.org/10.1029/2018GL077706>
- Cook, K. L., & Dietz, M. (2022). Seismic advances in process geomorphology. *Annual Review of Earth and Planetary Sciences*, 50(1). <https://doi.org/10.1146/annurev-earth-032320-085133>
- Eibl, E. P. S., Bean, C. J., Einarsson, B., Pálsson, F., & Vogfjörð, K. S. (2020). Seismic ground vibrations give advanced early-warning of subglacial floods. *Nature Communications*, 11(1), 2504. <https://doi.org/10.1038/s41467-020-15744-5>
- Ford, D., & Williams, P. D. (2007). *Karst hydrogeology and geomorphology*. John Wiley & Sons.
- Fores, B., Champollion, C., Mainsant, G., Albaric, J., & Fort, A. (2018). Monitoring saturation changes with ambient seismic noise and gravimetry in a karst environment. *Vadose Zone Journal*, 17(1), 170163–170212. <https://doi.org/10.2136/vzj2017.09.0163>
- Garambois, S., Voisin, C., Romero Guzman, M. A., Brito, D., Guillier, B., & Réffloch, A. (2019). Analysis of ballistic waves in seismic noise monitoring of water table variations in a water field site: Added value from numerical modelling to data understanding. *Geophysical Journal International*, 219(3), 1636–1647. <https://doi.org/10.1093/gji/ggz391>
- Gimbert, F., Tsai, V. C., Amundson, J. M., Bartholomaus, T. C., & Walter, J. I. (2016). Subseasonal changes observed in subglacial channel pressure, size, and sediment transport. *Geophysical Research Letters*, 43, 3786–3794. <https://doi.org/10.1002/2016GL068337>
- Gimbert, F., Tsai, V. C., & Lamb, M. P. (2014). A physical model for seismic noise generation by turbulent flow in rivers. *Journal of Geophysical Research: Earth Surface*, 119, 2209–2238. <https://doi.org/10.1002/2014JF003201>
- Hartmann, A., Goldscheider, N., Wagener, T., Lange, J., & Weiler, M. (2014). Karst water resources in a changing world: Review of hydrological modeling approaches. *Reviews of Geophysics*, 52, 218–222. <https://doi.org/10.1002/2013RG000443>
- Herman, E. K., Toran, L., & White, W. B. (2008). Threshold events in spring discharge: Evidence from sediment and continuous water level measurement. *Journal of Hydrology*, 351(1–2), 98–106. <https://doi.org/10.1016/j.jhydrol.2007.12.001>
- Hiltunen, D. R., & Cramer, B. J. (2008). Application of seismic refraction tomography in karst terrane. *Journal of Geotechnical and Geoenvironmental Engineering*, 134(7). [https://doi.org/10.1061/\(ASCE\)1090-0241\(2008\)134:7\(938\)](https://doi.org/10.1061/(ASCE)1090-0241(2008)134:7(938))
- James, S. R., Scream, E. J., Russo, R. M., Panning, M. P., Bremner, P. M., Stanciu, A. C., et al. (2017). Hydrostratigraphy characterization of the Floridan aquifer system using ambient seismic noise. *Geophysical Journal International*, 209(2), 876–889. <https://doi.org/10.1093/gji/ggx064>
- Kim, D., & Lekic, V. (2019). Groundwater variations from autocorrelation and receiver functions. *Geophysical Research Letters*, 46, 13722–13729. <https://doi.org/10.1029/2019GL084719>
- Krieger, S., Freij, N., Brazhe, A., Torrence, C., & Compo, G. P. (2022). PyCWT: Spectral analysis using wavelets in Python. Retrieved from <https://pycwt.readthedocs.io/en/latest/index.html>
- Lapins, S., Roman, D. C., Rougier, J., de Angelis, S., Cashman, K. V., & Kendall, J.-M. (2020). An examination of the continuous wavelet transform for volcano-seismic spectral analysis. *Journal of Volcanology and Geothermal Research*, 389. <https://doi.org/10.1016/j.jvolgeores.2019.106728>
- Lindner, F., Walter, F., Laske, G., & Gimbert, F. (2020). Glaciohydraulic seismic tremors on an Alpine glacier. *The Cryosphere*, 14(1), 287–308. <https://doi.org/10.5194/tc-14-287-2020>
- Luhmann, A. J., Bilek, S. L., Covington, M. D., Grapenthin, R., Woo, H. B., Gochenour, J. A., et al. (2023). Hydrologic (discharge, level, pressure, voltage, electrical conductivity, and temperature) and atmospheric (pressure and temperature) data from injection experiments and a rain event at Bear Spring, MN, USA, June 10–12, 2016, HydroShare. Retrieved from <http://www.hydroshare.org/resource/74a7fedb4f694ab6aafa3e6d6f47d129>
- Mayaud, C., Wagner, T., Benischke, R., & Birk, S. (2014). Single event time series analysis in a binary karst catchment evaluated using a groundwater model (Lurbach system, Austria). *Journal of Hydrology*, 511, 628–639. <https://doi.org/10.1016/j.jhydrol.2014.02.024>
- Megies, T., Beyreuther, M., Barsch, R., Krischer, L., & Wassermann, J. (2011). ObsPy—What can it do for data centers and observatories? *Annals of Geophysics*, 54(1), 47–58. <https://doi.org/10.3929/ethz-b-000130217>
- Midwestern Regional Climate Center. (2021). Retrieved from <https://mrcc.illinois.edu/CLIMATE/>
- Minnesota Department of Natural Resources. (2021). Minnesota annual precipitation normal: 1991–2020 and the change from 1981–2010. Retrieved from https://www.dnr.state.mn.us/climate/summaries_and_publications/minnesota-annual-precipitation-normal-1991-2020.html

- Minnesota Department of Natural Resources. (2022). *Minnesota karst features database*. Minnesota Department of Natural Resources, Groundwater Atlas Program. Retrieved from https://www.dnr.state.mn.us/waters/groundwater_section/mapping/springs.html
- Mossler, J. H. (2008). *Paleozoic stratigraphic nomenclature for Minnesota* (Vol. 65). Minnesota Geological Survey Report of Investigations.
- Nanni, U., Gimbert, F., Vincent, C., Gräff, D., Walter, F., Piard, L., & Moreau, L. (2020). Quantification of seasonal and diurnal dynamics of subglacial channels using seismic observations on an Alpine glacier. *The Cryosphere*, *14*(5), 1475–1496. <https://doi.org/10.5194/tc-14-1475-2020>
- Podolskiy, E. A. (2020). Toward the acoustic detection of two-phase flow patterns and Helmholtz resonators in englacial drainage systems. *Geophysical Research Letters*, *47*, e2020GL086951. <https://doi.org/10.1029/2020GL086951>
- Podolskiy, E. A., Fujita, K., Sunako, S., Tsushima, A., & Kayastha, R. B. (2018). Nocturnal thermal fracturing of a Himalayan debris-covered glacier revealed by ambient seismic noise. *Geophysical Research Letters*, *45*, 9699–9709. <https://doi.org/10.1029/2018GL079653>
- Quiros, D. A., Brown, L. D., & Kim, D. (2016). Seismic interferometry of railroad induced ground motions: Body and surface wave imaging. *Geophysical Journal International*, *205*(1), 301–313. <https://doi.org/10.1093/gji/ggw033>
- Ravbar, N. (2013). Variability of groundwater flow and transport processes in karst under different hydrologic conditions. *Acta Carsologica*, *42*(2–3). <https://doi.org/10.3986/ac.v42i2.644>
- Ronan, T. J., Lees, J. M., Mikesell, T. D., Anderson, J. F., & Johnson, J. B. (2017). Acoustic and seismic fields of hydraulic jumps at varying Froude numbers. *Geophysical Research Letters*, *44*, 9734–9741. <https://doi.org/10.1002/2017GL074511>
- Roeoeli, C., Walter, F., Ampuero, J.-P., & Kissling, E. (2016). Seismic moulin tremor. *Journal of Geophysical Research: Solid Earth*, *121*, 5838–5858. <https://doi.org/10.1002/2015JB012786>
- Rost, S., & Thomas, C. (2002). Array seismology: Methods and applications. *Reviews of Geophysics*, *40*(3), 1008. <https://doi.org/10.1029/2000RG000100>
- Schmandt, B., Aster, R. C., Scherler, D., Tsai, V. C., & Karlstrom, K. (2013). Multiple fluvial processes detected by riverside seismic and infrasound monitoring of a controlled flood in the Grand Canyon. *Geophysical Research Letters*, *40*, 4858–4863. <https://doi.org/10.1002/grl.50953>
- Sinha, S., Routh, P. S., Anno, P. D., & Castagna, J. P. (2005). Spectral decomposition of seismic data with continuous-wavelet transform. *Geophysics*, *70*(6), 19–25. <https://doi.org/10.1190/1.2127113>
- Smith, K., & Tape, C. (2019). Seismic noise in Central Alaska and influences from rivers, wind, and sedimentary basins. *Journal of Geophysical Research: Solid Earth*, *124*, 11678–11704. <https://doi.org/10.1029/2019JB017695>
- Sumanovac, F., & Weisser, M. (2001). Evaluation of resistivity and seismic methods for hydrogeological mapping in karst terrains. *Journal of Applied Geophysics*, *47*(1). [https://doi.org/10.1016/S0926-9851\(01\)00044-1](https://doi.org/10.1016/S0926-9851(01)00044-1)
- Torrence, C., & Compo, G. P. (1998). A practical guide to wavelet analysis. *Bulletin of the American Meteorological Society*, *79*(1), 61–78. [https://doi.org/10.1175/1520-0477\(1998\)079<0061:APGTWA>2.0.CO;2](https://doi.org/10.1175/1520-0477(1998)079<0061:APGTWA>2.0.CO;2)
- Vesper, D. J., & White, W. B. (2003). Metal transport to karst springs during storm flow: An example from Fort Campbell, Kentucky/Tennessee, USA. *Journal of Hydrology*, *276*(1–4), 20–36. [https://doi.org/10.1016/S0022-1694\(03\)00023-4](https://doi.org/10.1016/S0022-1694(03)00023-4)
- Vore, M. E., Bartholomaus, T. C., Winberry, J. P., Walter, J. I., & Amundson, J. M. (2019). Seismic tremor reveals spatial organization and temporal changes of subglacial water system. *Journal of Geophysical Research: Earth Surface*, *124*, 427–446. <https://doi.org/10.1029/2018JF004819>
- Welch, P. (1967). The use of fast Fourier transform for the estimation of power spectra: A method based on time averaging over short, modified periodograms. *IEEE Transactions on Audio and Electroacoustics*, *15*(2), 70–73. <https://doi.org/10.1109/TAU.1967.1161901>
- White, W. B. (2002). Karst hydrology: Recent developments and open questions. *Engineering Geology*, *65*(2–3), 85–105. [https://doi.org/10.1016/S0013-7952\(01\)00116-8](https://doi.org/10.1016/S0013-7952(01)00116-8)
- Worthington, S. R. (1999). A comprehensive strategy for understanding flow in carbonate aquifers. *Karst Modeling*, *5*, 30–37.
- Worthington, S. R. H., & Ford, D. C. (2009). Self-organized permeability in carbonate aquifers. *Groundwater*, *47*(3), 326–336. <https://doi.org/10.1111/j.1745-6584.2009.00551.x>
- Worthington, S. R., Ford, D. C., & Beddows, P. A. (2000). Porosity and permeability enhancement in unconfined carbonate aquifers as a result of dissolution. In A. V. Klimchouk, D. C. Ford, A. N. Palmer, & W. Dreybrodt (Eds.), *Speleogenesis: Evolution of karst aquifers* (pp. 220–223). National Speleological Society of America.
- Wright, S. J., Vasconcelos, J. G., & Lewis, J. W. (2017). Air–water interactions in urban drainage systems. *Proceedings of the Institution of Civil Engineers-Engineering and Computational Mechanics*, *170*(3), 91–106. <https://doi.org/10.1680/jencm.16.00024>
- Zhan, Z. (2019). Seismic noise interferometry reveals transverse drainage configuration beneath the surging bering glacier. *Geophysical Research Letters*, *46*, 4747–4756. <https://doi.org/10.1029/2019GL082411>